



Additive Manufacturing of Aqueous-Processed LiMn_2O_4 Thick Electrodes for High-Energy-Density Lithium-Ion Batteries

Lorenzo Airoldi,^[a] Umberto Anselmi-Tamburini,^[a] Barbara Vigani,^[b] Silvia Rossi,^[b] Piercarlo Mustarelli,^[c] and Eliana Quartarone^{*[a]}

Enhancing electrode areal capacity of lithium-ion batteries will result in cost saving and better electrochemical performances. Additive manufacturing (AM) is a very promising solution, which enables to build structurally complex electrodes with well-controlled geometry, shape and thickness. Here we report on 3D-printed cathodes based on LiMn_2O_4 (LMO) as the active material, which are fabricated by robocasting AM via aqueous processing. Such a technology is: i) environmentally friendly, since it works well with water and green binders; ii) fast, due to very short deposition times and rapid drying process because of low amount of solvent in the printable pastes; iii) easily scalable. The cathodes are produced by extruding pastes with

higher solid loadings ($> 70 \text{ vol\%}$) than those typically reported in literature. The printing efficiency is strongly affected by both the binder and the carbonaceous additive. The best cathode is composed by LMO, Pluronic as the binder, and a mixture of graphite/carbon black as the electronic conductor, which is critical for achieving optimal electrochemical performance. The cathode with thickness of $200 \mu\text{m}$ and mass loading of 13 mg cm^{-2} exhibits good electrochemical areal capacity (2.3 mAh cm^{-2}) and energy density ($> 32 \text{ J cm}^{-2}$). Our results may boost the development of greener, lower cost and more efficient new generation of LIBs for applications as household energy storage or even micro-battery technology.

1. Introduction

In order to allow full diffusion of the electric vehicles, the advanced storage systems must be competitive in terms of performances and costs. In the specific case of the next generation Li-ion (LIBs) or Li-metal batteries (LiBs), the expected energy density must be higher than 350 Wh kg^{-1} and 400 Wh kg^{-1} , respectively, with a cost lower than $100 \text{ US\$/KWh}$ at system level. These targets require focusing on new materials and innovative production technologies of both components and cells (see for instance E. Commission, "SET-Plan Action 7 – Implementation Plan, 2017). The battery energy density can be enhanced by using high-voltage cathodes and Silicon-Carbon composite anodes, even if the final step will be assured by Li metal anodes, which, in turn, open the way to more performing chemistries, as Li-air and Li–S.^[1–7]

In addition to the possibility of playing with anode and cathode materials, a further way to improve battery perform-

ance is the reduction in weight and volume of non-active materials, such as current collectors and packaging. In this context, an important route is the fabrication of thick electrodes. In fact, a conventional roll-to-roll coating of a solvent-based slurry onto the metallic current collector can give $20\text{--}30 \mu\text{m}$ thin electrodes, where the active material loading is less than 5 mg cm^{-2} .^[8] The possibility to fabricate electrodes in the range of few hundred microns will allow loadings of several dozens of milligrams per square centimeter, where the relative amount of the non-active materials is significantly reduced.^[9] By this approach it could be possible to increase the energy density and to reduce the fabrication costs.^[10–12]

Thick electrodes, however, cannot be simply prepared on metal current collectors because of important issues, such as: i) tendency to fracture and delaminate from the metallic support during the conventional coating, ii) the low porosity and difficulty of the electrolyte to penetrate through the electrode, iii) higher charge transfer resistance due to the longer distance from the electrolyte to the current collector and, iv) consequent poor charge transfer kinetics, leading to worse current rates.^[9,11]

Recently, new technologies for materials engineering enabled the fabrication of electrode architectures with low tortuosity connecting pathways, properly engineered pores and/or new local geometries, where the amount of electrochemically active compound is significantly increased.^[9] Among them, 3D printing, also known as additive manufacturing (AM), is an emerging tool enabling the building of complex objects with well-controlled geometry through a layer-by-layer deposition process.^[13] Several reviews recently appeared in literature showing the feasibility of 3D printing as a successful technology in electrochemical energy storage (EES), and specifically in

[a] L. Airoldi, U. Anselmi-Tamburini, Dr. E. Quartarone
Department of Chemistry and INSTM,
University of Pavia
Via Taramelli 16, 27100 Pavia, Italy
E-mail: eliana.quartarone@unipv.it

[b] B. Vigani, S. Rossi
Dipartimento di Scienze del Farmaco,
Università di Pavia
Via Taramelli 6, 27100 Pavia, Italy

[c] P. Mustarelli
Department of Materials Science,
University of Milano Bicocca and INSTM
Via Cozzi 55, 20125 Milan, Italy

 Supporting information for this article is available on the WWW under
<https://doi.org/10.1002/batt.202000058>

the battery field. Many advantages were found in comparison to the conventional roll-to-roll manufacturing process, e.g. a fine chemistry control, the possibility to fabricate on-chip EES devices or even the whole device with optimal thickness, up to millimeters, with enhanced areal capacitance and high energy density.^[14–19]

A number of thick cathodes and anodes, mostly based on LiFePO₄ and Li₄Ti₅O₁₂ respectively, were fabricated by means of different 3D printing approaches, including ink writing, direct writing, fused deposition modeling, stereolithography and paste extrusion. In most cases, high areal capacity values were observed, depending on key parameters like solid loading in the ink, deposition patterns, electrode components, number of deposited layers and resulting thickness.^[14,19–24]

Despite of the great potential of these technologies in the fabrication of thick electrodes, the commercialization of 3D-printed LIBs is still far away, and the albeit attractive results are still limited to the lab-scale. More work is required to address some crucial aspects of the deposition process, including materials selection, printing resolution and speed, and slurry formulation. Indeed, the active components of battery electrodes are typically based on ceramic phases, which are difficult to be processed by AM because of their high melting and sintering temperatures. For this reason, AM of ceramic materials is still quite limited.

Inside the wide family of AM processes, ceramic robocasting is well suited for electrode fabrication because it allows layer-by-layer deposition of ceramics and composites from pastes or highly loaded colloidal slurries, containing at least 65 vol % of powder, 35 vol % of solvent (usually water) and few percent of organic components.^[25–28] Robocasting have several advantages, which are hardly achievable by concurrent AM techniques, including: i) low cost, ii) flexibility in printer customization, iii) high resolution depending on the needle size, iv) versatility to deposit a wide selection of materials, by using both aqueous and non-aqueous solvents, within any 3D spatial position and complex geometries; v) intermediate-to-high printing speed. However, to be deposited by robocasting, the slurries must exhibit well-defined rheological parameters, as good shear thinning properties, viscosity during printing ranging from 10 and 100 Pa s and a shear elastic modulus between 0.1 and 10 MPa.^[27,28] It is mandatory to prepare ceramic slurries with high solid loading and minimal liquid content, while still maintaining favorable rheological properties. This can be achieved by proper balancing of key-factors like paste formulation and ceramic particle size.^[27] Although ceramic robocasting was widely employed in the production of various ceramic objects, it is still poorly explored in the fabrication of thick composite electrodes for LIBs. Only few studies discussed the enhanced areal capacity of robo-casted cathodes for LIBs based on Li–Mn oxides. Here, the electrodes were prepared by using conventional inks including polyvinylidene fluoride (PVDF) as the binder and N-methyl-pyrrolidone (NMP) as the dispersant.^[29,30]

In this paper we report on the AM fabrication, via ceramic robocasting technology, of thick electrodes based on LiMn₂O₄ (LMO) as cathodes for high-energy LIBs. Our key point, here, is

that the electrodes were deposited, for the first time to our best knowledge, from water-based, highly loaded slurries by using eco-friendly binders. The printable pastes were optimized by exploring different carbonaceous materials (graphite, multi-walled carbon nanotubes and carbon black) as conducting carbons, and carboxymethylcellulose (CMC) and Pluronic P-123 as the binders. We tested several solid loadings in order to achieve the best rheological behavior for a successful printing.

Experimental Section

Preparation of the LMO-based pastes

Pastes with different solid loadings have been prepared by using two binders (Pluronic P-123 (PL) and carboxymethylcellulose-Na salt (CMC)) (Sigma-Aldrich), and three carbonaceous materials also mixed together: Graphite KS10 (Imerys Graphite and Carbon), carbon black Super C65 (Imerys Graphite and Carbon), and multi-walled carbon nanotubes (MWCNTs, VWR). Commercial LiMn₂O₄ particles were used as the active materials (Selectipur SP30). The paste composition for each printed system is reported in Table 1.

The pastes were prepared by mixing the proper amounts of LiMn₂O₄ and carbon in a zirconia jar with a high energy planetary ball miller (HEBM, Fritsch Pulverisette 7). Two milling cycles of 10 min were carried out at 150 rpm with a pause of 5 min. The powder/sphere ratio was kept at 1:20. The binder was subsequently added by taking the right volume of a polymer in water solution at known concentration (see Table 1). The paste was manually mixed, then transferred in two connected syringes, and further homogenized by pumping it several times (at least 10 times) from a syringe to another. Finally, it was introduced in the extrusion apparatus, as sketched in Figure 1.

Robocasting process

The LMO-based pastes were used to fabricate 3D electrodes by means of a home-customized inverted “delta” printer, equipped with a paste-extrusion head, as reported in Figure 2. The printing

Table 1. Paste formulation of all the prepared samples with different binders and carbonaceous components. The relative amounts are expressed as weight percent (SL wt %) and volume percent (SL vol %) of the solid components, respectively, and the total solid amount per solvent volume (SL g mL⁻¹). G10 and MC are the samples with the best rheological properties, which were later used for 3D printing. In the samples PL/(KS10 + C65) the ratio KS10:C65 is 2:1 w/w. Other abbreviations are reported in the next section describing the robocasting process.

Binder/carbon	SL [wt %]	SL [Vol %]	SL [g mL ⁻¹]
CMC/C65	29	49	0.4
PL/C65	54	75	1.3
PL/C65	69	74	2.1
PL/MWCNTs	69	50	2.1
PL/KS10			
A	79	84	3.5
B (G10)	68	76	2.1
C	64	72	1.7
D	59	68	1.4
PL/(KS10+C65)			
A	79	88	3.8
B (MC)	74	85	2.8
C	69	81	2.2
D	64	78	1.8
E	59	74	1.4

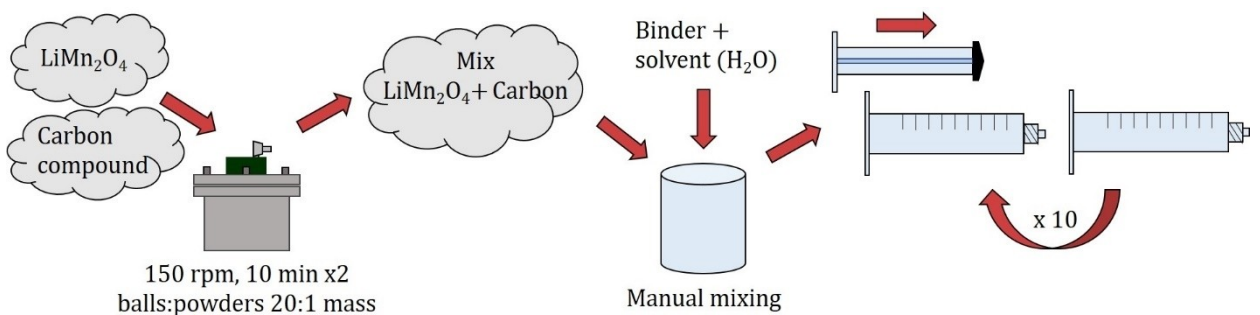


Figure 1. Steps of the whole process for paste preparation

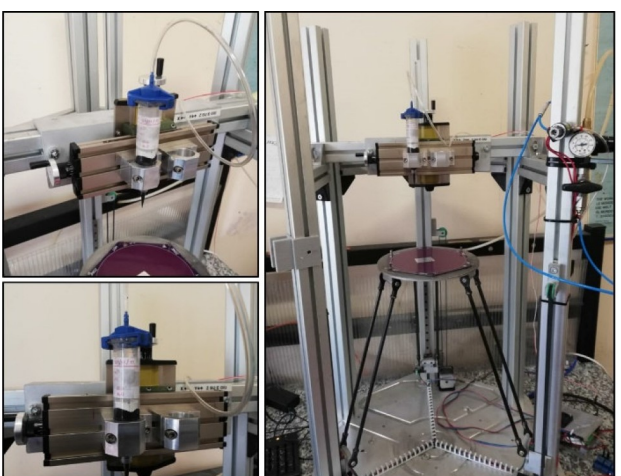


Figure 2. Software and hardware devices of the home-customized inverted DELTA printer, used for the 3D electrode fabrication.

process was controlled by means of specific software packages: i) CAD program for the geometrical model creation and conversion of the drawing file to a stereolithography "STL" format to be readable by the printing machine; the 3D model of the part was sliced to thin sections which were printed layer by layer on the printing platform; ii) 3D Builder for the real 3D structure build-up; iii) Slic3r and Repetier Host to manage the printer, the XY axes movements and to control each printing step, the model slicing and the temperature of both supporting stage and nozzles. In order to properly print the selected pastes, it was strictly necessary to find an optimal compromise among several experimental factors as printing speed, extrusion pressure and syringe needle, taking into account the observed ink rheological behavior. Similar values of printing speed were chosen to define the object boundaries as well as to infill it.

In more detail, the slurry was placed in 30 cm³ syringe, which was connected to a controlled pneumatic fluid dispersion tool enabling a printing extrusion pressure up to 5 bar. Plastic SmoothFlow nozzles with different diameters (0.45 mm, 0.24 mm and 0.20 mm, EFD Optimum, Nordson) were adopted for the deposition process. The printing speed was varied between 5 mm s⁻¹ and 25 mm s⁻¹, depending on the ink rheological properties. The paste was deposited directly onto a 30 µm-thick Al foil (the current collector), which was kept fixed on the printer stage. First, a base layer was deposited onto the metallic foil; then the interdigitate structure was printed on it to enhance the surface area. The resulting electrode was dried at 80 °C overnight and finally transferred in a glove box for the cell assembly.

Materials characterization.

X-rays diffraction (XRD) patterns of the active material (LiMn₂O₄) and the composite system (LMO/C/Binder after aqueous process) were collected by means of a Bruker Advance D8 diffractometer (Cu-K α radiation, $\lambda = 0.154$ nm) using an Al sample holder. The pattern was acquired in the 20 range from 15° to 60°, with scan step of 0.02° and a fixed counting time per step of 4 s.

SEM analyses on the electrode components and on the post-mortem cathode were performed using a Tescan Mira3XMU microscope operated at 20 kV and equipped with an EDAX EDS analysis system. The samples were coated with a carbon thin film using a Cressington 208 carbon coater.

Rheological analyses were performed by means of a rotational rheometer (MCR 102, Anton Paar, I) equipped with a parallel plate combination (PP50, diameter = 50 mm) as measuring system. The measurement gap was set at 1.5 mm. Sample viscosity was measured at increasing shear rates in the range 10–1000 s⁻¹ at 25 °C. The spur value and the dynamic yield stress were identified for each sample where possible. Three replicates ($n=3$) were considered for each sample.

Sample viscoelasticity was assessed by dynamic oscillatory measurements. In the stress sweep test, increasing stresses were applied at a constant frequency (1 Hz) and the elastic response of the sample, expressed as elastic (G') and loss (G'') modulus, was measured. In the oscillation test, a shear stress, chosen in the linear viscoelastic region previously determined with the stress sweep

test, was applied at increasing frequencies (1 to 10 Hz) and G' and G'' profiles were recorded. Measurements were performed at 25 °C in triplicate.

Electrochemical tests

The electrochemical characterization of the 3D printed electrodes was performed by means of cyclic voltammetry, galvanostatic cycling and electrochemical impedance spectroscopy, by using Swagelok-type cells assembled in an Argon filled-glove box (H_2O and O_2 below 0.5 ppm) with Li foil as counter and reference electrode. Electrodes were separated with a Whatman glass fiber separator, soaked in a commercial solution of 1 M LiPF₆ in EC:DMC (50:50 vol%). The cells were cycled on a Biologic BCS 810 battery tester from 3 V to 4.9 V. All the potentials reported refer to the Li⁺/Li couple.

The impedance on the cells was measured by means of Electrochemical Impedance Spectroscopy at room temperature, using a Frequency Response Analyzer (FRA) (Solartron 1255) connected to an Electrochemical Interface (Solartron 1287), by applying an AC voltage of 100 mV in the frequency range between 0.1 Hz–1 MHz.

2. Results and Discussion

2.1. Paste Optimization: Role of the Components and Rheologic Behaviour

The printable pastes were prepared by selecting LiMn₂O₄ as the standard active material, and by developing an aqueous process to enable the use of green binders and to avoid toxic solvents (e.g. NMP). To this aim, several parameters were investigated during the slurry preparation, as the nature of polymer binder and carbonaceous additive, and the overall solid loading. These parameters were tested in order to achieve suitable rheological properties, which are critical for the robocasting process and for an optimal control of the object shape.

2.1.1. LMO Compatibility with the Aqueous Process

LMO is a commercial product. It was first characterized from a morphological and microstructural point of view in order to evaluate its stability in water. Figure S1 reports the SEM analysis of the pristine LMO. The images evidence aggregation of squared particles with dimensions ranging between 90 and 500 nm, which are assembled in concentric shells. The material is pure and well crystallized, as demonstrated by the XRD pattern reported in Figure S2. The prolonged treatment in water and the mixing by ball milling with the other components did not affect the structure of the spinel, as proved by the related XRD patterns where no changes were detected before and after the treatments.

2.1.2. Selection of Water-Processable Binders

As the binder is expected to have a major impact on the rheological properties of the slurry, we initially compared the two water-soluble polymers, PL and CMC, while keeping fixed the carbon-based additive (Super C65), by preparing two pastes with the LMO:binder:C65 weight ratio of 70–20–10 wt%. Figures 3a–b show the behavior of shear stress vs. shear rate, and the real (G', elastic) and imaginary (G'', loss) components of the shear modulus vs. the shear stress. Basically, both pastes have a shear thinning behaviour. At high shear rates, the shear stress values of the two samples are comparable (Figure 3a). In contrast, at lower shear rates, in the typical range for printing (10–100 s⁻¹), the PL-based paste shows higher shear stress. Furthermore, contrary to CMC-system, in case of Pluronic ink, there is the clear evidence of a spur, which provides a static yield stress of about 800 Pa. Such spur is an index of high three-dimensional network in the suspension^[31] and, consequently, of a stronger ink structure at room temperature, which is highly desired in case of 3D printing processes. This aspect is related to the chemical structure of the Pluronic-based

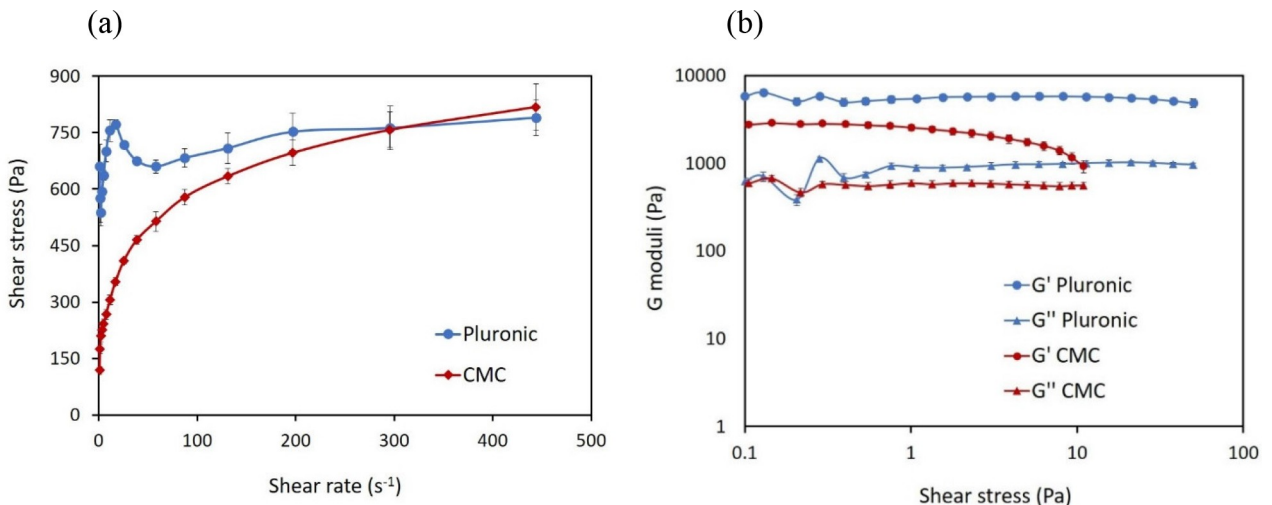


Figure 3. Shear stress (a) and G moduli at 1 Hz (b) profiles, measured at 25 °C, of CMC and PL inks (mean values \pm s.d.; $n = 3$). The G profiles errors are of the order of the symbol dimension.

polymers. Basically, PL is a poloxamer (PEO-PPO-PEO). It consists of two different polymers, hydrophilic PEO (polyethylene oxide) and hydrophobic PPO (polypropylene oxide), which attract each other in presence of water, creating micelles. Once formed, the micelles aggregate and bind more water, hence giving a gel. The presence of a 3D network facilitates the flow of the paste through fine deposition nozzles and contributes to preserve the 3D shape and integrity of the deposited pattern.^[32]

Figure 3b shows that in both cases the elastic component of the complex shear modulus is higher than the viscous one. However, the PL-based ink is characterized by higher G' values with respect to the CMC-based one, which is an index of better performances in the printing process. Therefore, for all these reasons (namely paste higher elastic component and 3D network), PL resulted more suitable as binder for the AM process, and was consequently selected as the polymer component for further studies.

In the next step, we investigated the influence of the carbon-based additive on the rheological properties of the slurry. Having fixed the binder, we tested MWCNTs, C65, KS10 and a mixture of C65 and KS10 (1:2 in weight). Figure 4 compares the images of four different printed electrodes, containing the same weight concentration of active material (LMO), carbon and PL binder (70/20/10 wt%). The nature of the additive significantly affects the layer adhesion to the current collector as well as the particles cohesion and, consequently, the layer integrity.

More in detail, MWCNTs was not suitable for AM printing, as it caused system pulverization over drying (Figure 4a). Lack of cohesion and adhesion to the substrate was also observed in case of Super C65, which also induced serious surface cracking (Figure 4b). In contrast, the use of graphite KS10 enables good-quality printed patterns, without any cracks or lack of adhesion to the Al substrate (Figure 4c). Similar results were obtained for the sample employing the mixture C65/KS10 (fig.4d), which exhibited well-defined geometry and undamaged shape.

Such a different behaviour was due to the morphology and microstructural parameters of the additives, as surface area, crystallinity, particles dimension, and aspect ratio (see Table S1a). In case of MWCNTs, their high aspect ratio (~375) did not allow homogeneous dispersion and good interaction with the other ink components. Super C65 had smaller particles and higher surface area than KS10 (see Table S1 and Figure S3), and

likely acted as a molecular sieve by absorbing a significant fraction of water-polymer solution, so subtracting the binder from the paste, and reducing particles cohesion and adhesion onto the metallic substrate. For this reason, only the pastes including KS10 and the KS10-C65 mixture were considered for the final rheological investigation and the printing process (samples PL-KS10 A-D and PL-KS10/C65 A-E of Table 1).

Figure 5 reports the viscosity behaviour of the pastes based on KS10 and KS/C65 additives. In particular, the graphs 5a and 5b compare the viscosity profiles vs. the shear rate of each composition at different solid loadings. All the inks under investigation (PL-KS10 A-D and PL-KS10/C65 A-E series) show shear thinning behaviour and their viscosity decreases by increasing the shear rate. As expected, the higher the solid loadings the higher sample viscosity, as evidenced in Figure 5c, where the specific values at 40 s⁻¹ are plotted against the solid loading SL wt%. The viscosity increase is almost linear, especially in case of the PL-KS10/C65 samples, where values between 0.35 and 100 Pa.s were observed in the range 59–79 wt%.

Despite of the use of different carbon-based additives, similar viscosity behaviours were observed among the two groups of samples for similar solid loadings. Figure S4 shows, as an example, the viscosity vs. shear rate plots for PL-KS10 B (SL = 68 wt%) and PL-KS10/C65 B (SL = 74 wt%). In this case, the values are nearly overlapping in the overall shear rate range between 1 and 100 s⁻¹, achieving viscosity of about 16 Pa.s at 40 s⁻¹. Therefore, a proper selection of components and compositions allow to make pastes with high SL, which are suitable for printing thick electrodes with high mass loading of active material. Because of a good compromise between viscosity and solid loading, the two compositions PL-KS10 B (SL = 68 wt%) and PL-KS10/C65 B (SL = 74 wt%) were selected for the electrode 3D printing. In the following these compositions, highlighted in bold in Table 1, will be named as G10 and MC, respectively.

Figure S5a–b shows the shear stress vs. profiles of G10 and MC inks. Although less evident in case of the paste based on the carbons mixture (MC), both the systems are characterised by the presence of a spur at lower shear rates (<100 s⁻¹), which is an index of tri-dimensional structure.^[31] Since the spur provides the static yield value, namely the stress value needed to break the sample structure before a significant flow occurs, the higher the stress value of the spur, the stronger the 3D

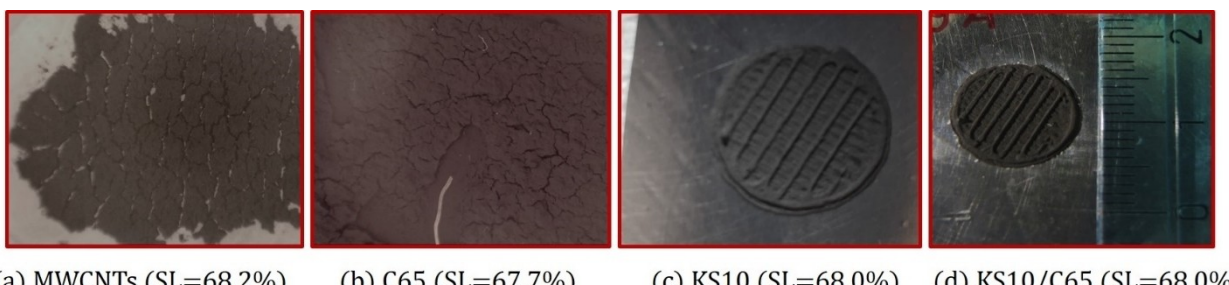


Figure 4. Images of the printed electrode pastes with different carbon-based additives

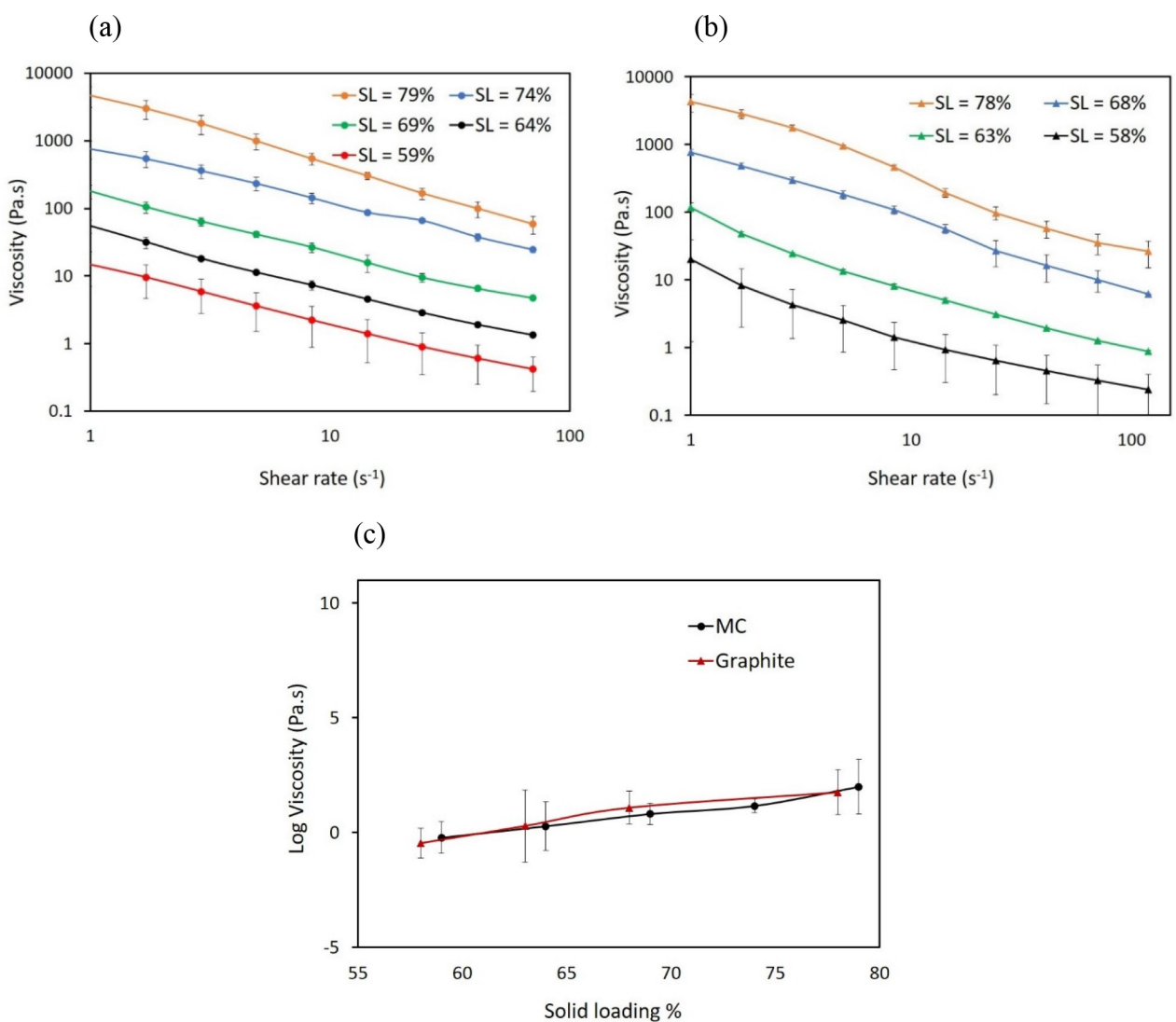


Figure 5. Log–viscosity vs. shear rate profiles of the PL-KS10 A–D (a) and PL-KS10/C65 A–E series (b), measured at 25 °C (mean values \pm s.e.; $n=3$). (c) Viscosity values, measured at 40 s⁻¹ and 25 °C, vs. the solid loading (mean values \pm s.e.; $n=3$).

structure. Table 2 reports the spur and the dynamic yield stress values of PL-KS10 A–D and PL-KS10/C65 A–E inks. It is noticeable that the spur position increases with the solid loading, suggesting a strengthening of the paste inner

structure. A similar trend is also evident for the dynamic yield stress, namely the minimum stress required for maintaining flow, which is calculated as the intercept on the y-axis of the straight line fitting the last points of the flow curve.

In case of KS10, no spur is evident at the lowest solid loading (59 wt%), which means that the paste flows in the whole explored shear rate range. In contrast, the KS10/C65-based samples exhibit static yield stress only for SL > 70 wt%. Finally, all the investigated pastes show an elastic behaviour prevailing on the viscous one, as confirmed by the stress sweep tests. In such experiments storage moduli (G') profiles higher than the loss one (G'') were ever collected (see Figure S6).

2.2. Electrode Structure

As stated before, two pastes were used in the electrode printing process, namely G10 ($SL = 68$ wt%) and MC ($SL = 74$ wt

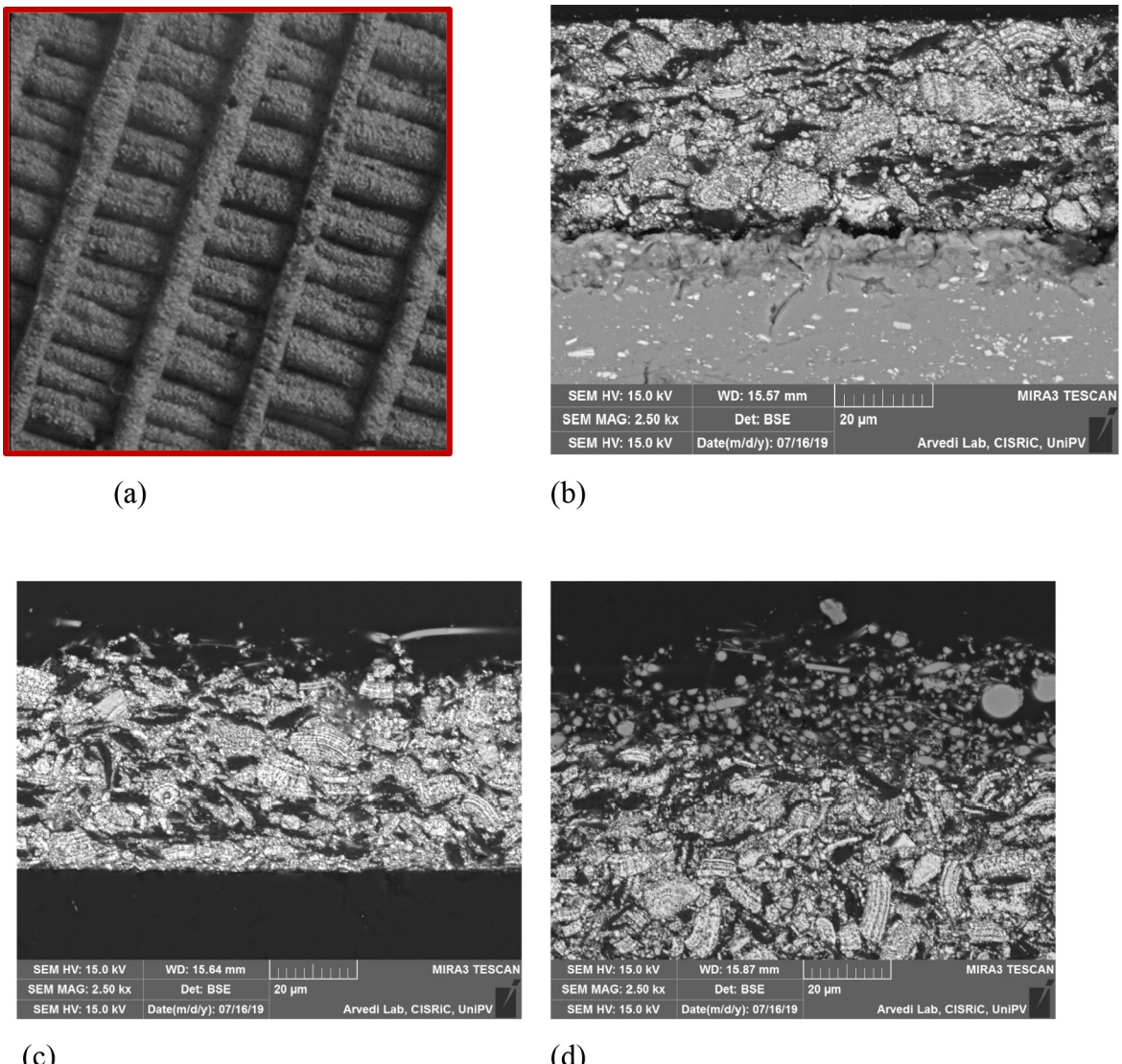
Table 2. Spur and dynamic yield stress values for PL-KS10 and PL-KS10/C65 inks at different SL% (mean values \pm s.e.; $n=3$). n.s.: no evident spur.			
Binder	SL [wt%]	Spur value [Pa]	Dynamic yield stress [Pa]
PL-KS10			
A	79	5163 \pm 249	2079 \pm 116
B (G10)	68	906 \pm 91	640 \pm 70
C	64	119 \pm 10	67 \pm 6
D	59	n.s.	7 \pm 1
PL-KS10/C65			
A	79	5259 \pm 965	4066 \pm 610
B (MC)	74	816 \pm 127	604 \pm 72
C	69	n.s.	204 \pm 19
D	64	n.s.	58 \pm 5
E	59	n.s.	18 \pm 2

%), which were optimized in terms of rheological properties. These inks exhibited strong adhesion among the electrode components and no evident shrinkage of the electrode material during the drying step. The printed electrodes were designed into parallel lines, 400 µm large and 1200 µm spaced, as already shown in Figure 4c-d, and highlighted in the optical microscopy image reported in Figure 6a.

The electrodes thicknesses were 60 ± 8 and 200 ± 15 µm for the G10 and MC pastes, respectively. Both the samples were porous, as evident from the SEM cross-sectional image of G10 shown in Figure 6b. A similar morphology was obtained for MC (not shown). The microscopic analysis shows pores diameters up to 20 µm, resulting from the evaporation of the solvent during the vacuum drying process. The electrodes porosity was determined by the ratio between the electrode actual density and the value reported in the literature for a highly densified commercial LMO electrode with similar composition

(2.83 g cm^{-3}).^[33] The pore volumes resulted of 47 vol % MC and 53 vol % for G10.

The active area of the printed electrodes was estimated from geometrical calculations, by considering diameter, number, length and spacing of the texture lines. A value of about 1.5 cm^2 was obtained for both the cathodes, which corresponds to a significant increase of the 3D electrodes surface area of ~50% over the $25 \pm 3 \mu\text{m}$ -thick sample prepared by conventional tape-casting. The microstructure of both cathodes remained almost intact on cycling (up to 35). Figure 6c-d shows the post-mortem cross-sectional SEM images of G10 (c) and MC (d) electrodes.



2.3. Electrochemical Behavior of the 3D-Printed Electrodes

The electrochemical performances of the G10 and MC printed electrodes were investigated on Swagelok-type cells in two-electrodes configuration by galvanostatic cycling and electrochemical impedance spectroscopy. The functional properties were compared with those observed in case of a composite film obtained from conventional tape-casting, whose data are reported in Figure S7a-d.

The areal mass loadings were 5 mg cm^{-2} and 13 mg cm^{-2} for the G10 and MC printed electrodes, respectively. The rate capability for both the electrodes was investigated at 0.1, 0.2 and 0.5 C (10 cycles at each C-rate). The intercalation/deintercalation steps of the electrodes were preliminary checked by evaluating the differential capacity from galvanostatic cycling at 0.05 C. Similar behaviors were obtained for both the printed electrodes. Figure S8 reports as an example the dQ/dV values vs V of the MC cathode. The characteristic peaks of LiMn_2O_4 were observed at 4.0 V and 4.2 V in the anodic plot and at 3.9 V and 4.1 V in the cathodic one. The electrochemical results confirm that lithium is extracted from the tetrahedral sites of the spinel structure at about 4 V in a two-stage process, which is typical of the LiMn_2O_4 electrode. As known from the literature, such two-step extraction, separated by less than 200 mV, is due to ordering the Li^+ ions on one half of their tetrahedral sites.^[34]

Figure 7 compares the electrochemical behavior of the G10 and MC electrodes, including rate capability, voltage profiles at different C-rates and charge/discharge at 0.1 C for about 30 cycles. Both the gravimetric (Figure 7a-b) and areal capacities are reported (Figure 7c-d). In the case of G10 cathode, the charge-discharge performance was poor. The specific capacity was about 85 mAh g^{-1} at low C-rate and abruptly decreased to about 40 mAh g^{-1} at 0.5 C (Figure 7a). The areal capacity was 0.44 mAh cm^{-2} , less than a factor of two higher than the corresponding value of the much thinner cast electrode ($C = 0.26 \text{ mAh cm}^{-2}$) (Figure 7c). When the current density changed back to 0.1 C the capacity again increased only to 79 mAh g^{-1} , so indicating not complete reversibility. When cycled for longer times at 0.1 C the capacity retention was in the range 96–98% for about 30 cycles (Figure 7g). Moreover, an overpotential in the charge/discharge processes and some trend instability were observed, which likely suggested a not optimal electron and ion transport across the electrode (Figure 7e-g).

Instead, in case of MC printed electrode, much better performances were observed, with specific capacity of 113 mAh g^{-1} at 0.1 C, 103 mAh g^{-1} at 0.2 C and 95 mAh g^{-1} at 0.5 C (Figure 7b). The capacity decrease by increasing the current density is indeed much lower than that obtained for the G10 electrode (21% vs. 58%), despite of the greater electrode thickness. The charge/discharge plateaus are quite flat, specially at lower current density, and the polarization is significantly smaller than that showed by the G10 electrode (Figure 7d-f). The capacity delivered at 0.1 C is very stable and almost constant values of about 115 mAh g^{-1} are reversibly maintained for more than 30 cycles with a coulombic efficiency very close to unit (Figure 7h).

This clearly indicated a better charge transfer kinetics of the electrode with the graphite/carbon black mixture. In this case average areal capacity of 2.3 mAh cm^{-2} , 2.1 mAh cm^{-2} , 1.9 mAh cm^{-2} were obtained in the explored C-rate range, that is about one order of magnitude higher than that of the conventional tape-casted electrode (Figure 7d). A comparable areal capacity can be found in very few reports on LMO-based electrodes.^[29,30] In particular LiMn_2O_4 -based electrodes were printed from optimized pastes with 30 vol% of solid loading by means of AM process assisted by an electric field. In this case specific and areal capacity of 92 mAh g^{-1} and 3 mAh cm^{-2} were obtained for $270 \mu\text{m}$ - thick cathode, whereas superior performances (117 mAh g^{-1} and 4.5 mAh cm^{-2}) were achieved by the same researchers by enhancing the electrode thickness up to about $400 \mu\text{m}$. However, such values are referred to electrodes obtained from pastes including PVDF and NMP, with different amount of active material, lower solid loading (up to 30–35 vol%) and consequently higher amount of toxic solvent.

The superior performance of the MC cathode is likely related to the carbonaceous additive. This is based on a mixture of graphite and carbon black, the latter one likely favoring the formation of a better percolative conducting network, which positively affects the rate performance. The MC electric conductivity, measured by impedance spectroscopy, is, in fact, more than twice that of G10 ($\sigma_e = 10$ and 4.5 mS cm^{-1} , respectively). Although the electrodes have the same 3D geometry, the MC electrode shows a better wettability due to the presence of Super C65, which is more porous and has higher surface area than graphite KS10 (see Table S1). This favors a better electrolyte penetration into the composite, which facilitates the electron/ion diffusion, even in case of a thicker sample, thus avoiding ion accumulation on the surface. Another positive effect is the formation of a stable interphase, which could slow undesirable reactions, e.g. those responsible of active material dissolution. A microscopic evidence of the formation of such interphase is given by post-mortem SEM analysis. The MC sample shows a porous layer made of particles with different shape and size, which spread all over the electrode surface (Figure 6d). This is not observed in the G10 electrode (Figure 6c).

These microstructural features, and their relationships with electrode charge transfer and diffusion, were further investigated by electrochemical impedance spectroscopy. Figure 8 shows the Nyquist plots of the two electrodes, obtained at open circuit voltage (OCV) after the galvanostatic cycling. The overall shapes of the spectra were different. The G10 electrode showed a semicircle in the high frequency domain (charge transfer contribution) followed by a linear region with a slope of about 45° , which is likely related to the charge diffusion (Warburg contribution). The MC electrode showed two distinct semicircles at high and middle frequency, due to charge transfer and to interphase observed in the SEM image of Figure 6d, respectively, followed by the Warburg contribution. The impedance spectra were fitted by using the equivalent circuit reported in the inset of Figure 8. Table 3 reports some of the best-fit parameters. It may be observed that the charge transfer resistance, R_{ct} , is significantly different between the two

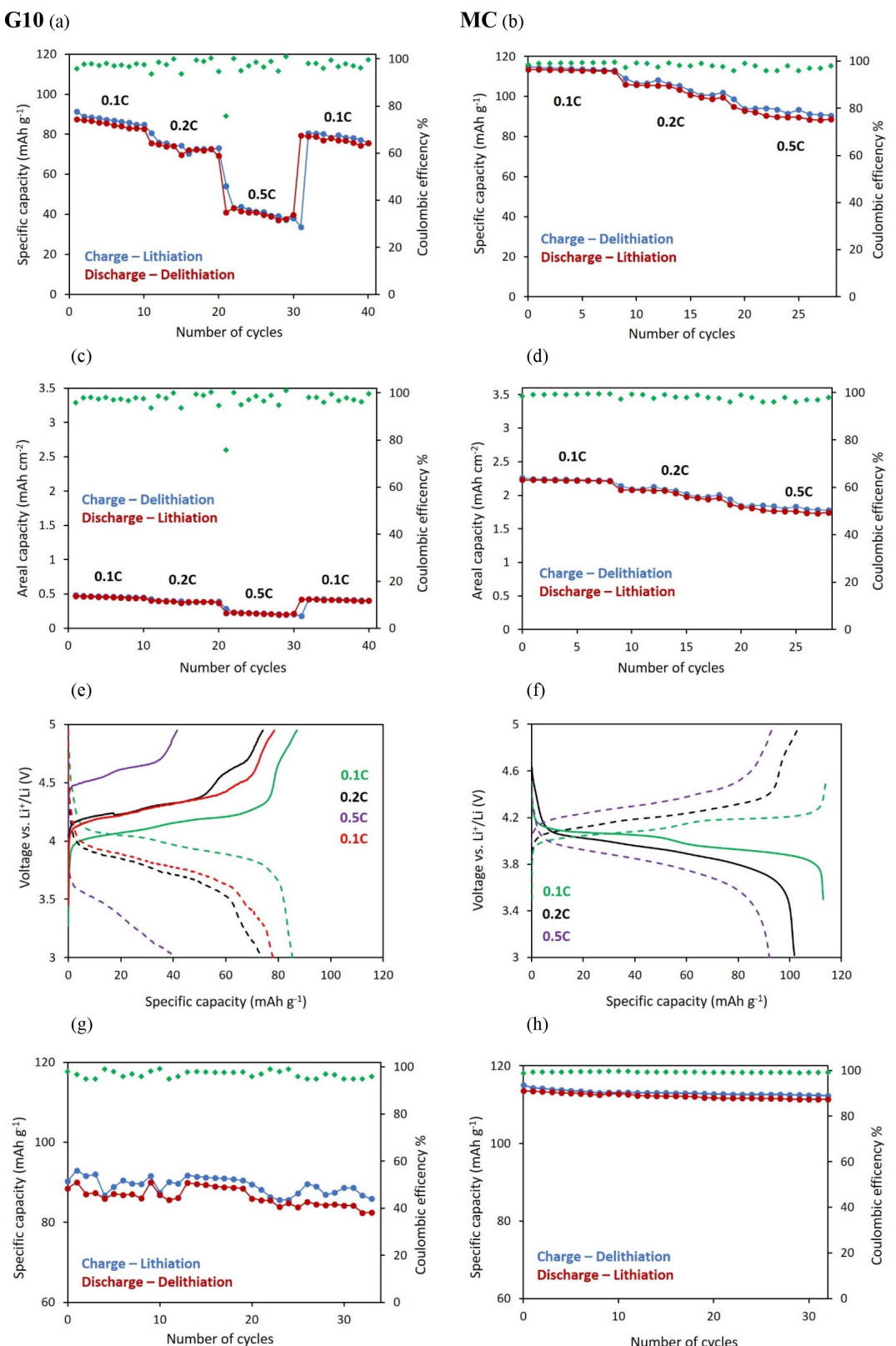


Figure 7. a-b) Specific capacity; c-d) areal capacity; e-f) voltage profiles, and g-h) cycling stability at 0.1 C of the cells G10/LiPF₆-EC-DMC/Li and MC/LiPF₆-EC-DMC/Li, respectively.

electrodes, being equal to 94 and 396 Ωcm^2 for MC and G10, respectively.

This could be explained by taking into account the presence, in the MC electrode, of Super C65 in addition to KS10

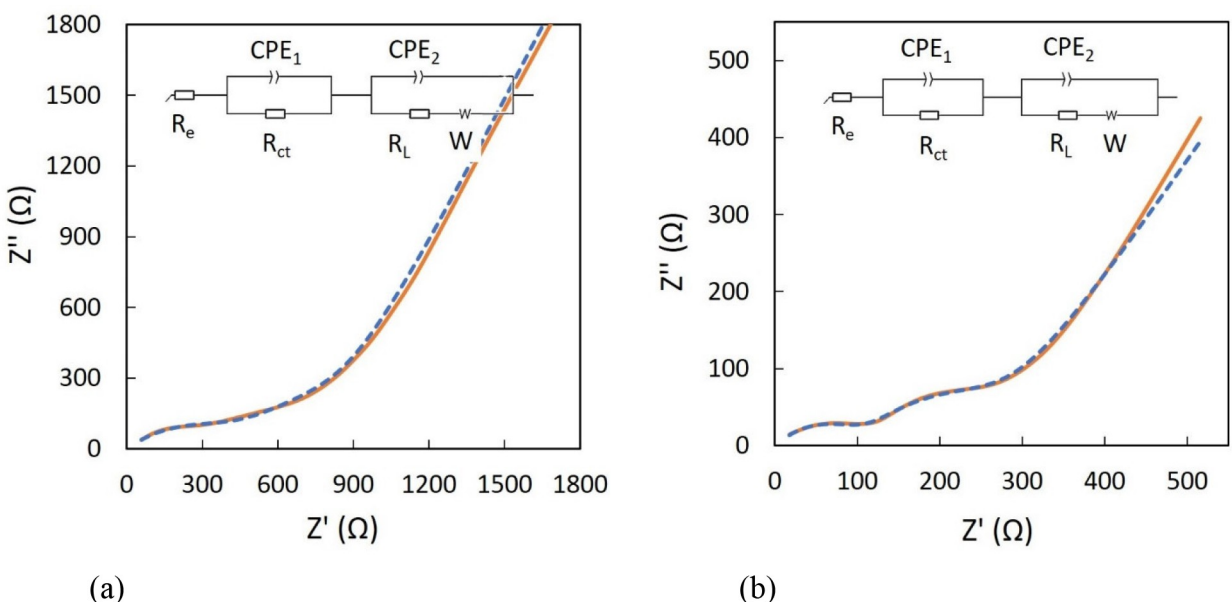


Figure 8. Nyquist plots collected at OCV after galvanostatic cycling for a) G10-based half-cell; b) MC-based half-cell. The inset reports the equivalent circuit models used for the spectral best-fitting analysis.

Table 3. Fitting parameters of the Nyquist plots collected by electrochemical impedance spectroscopy on half-cells based on G10 and MC cathodes.

	R_{Ω} [Ωcm^2]	R_{ct} [Ωcm^2]	R_L [Ωcm^2]	σ_w [$\Omega s^{-1/2}$]	D_{Li+} [$10^{-13} \text{ cm}^2 \text{s}^{-1}$]
G10	3.7	396	—	516	0.19
MC	2.7	94	102	105	1.85

graphite. The two electrodes also showed different diffusive behavior, and then different Warburg impedances, Z_w , and Warburg coefficients, σ_w , which may be computed by impedance spectroscopy through the use of the following equations [Eqs. (1), (2)]:^[35]

$$Z_w = \frac{\sigma_w}{\omega^{1/2}} - j \frac{\sigma_w}{\omega^{1/2}} \quad (1)$$

and

$$\sigma_w = \frac{RT}{n^2 F^2 A \sqrt{2}} \left(\frac{1}{D_o^{1/2} c_o^b} + \frac{1}{D_r^{1/2} c_r^b} \right) \quad (2)$$

where A is the electrode area, c_o^b and c_r^b the bulk concentration of the oxidized and reduced species, respectively, and D_o and D_r the corresponding diffusion coefficients. From these equations, it is possible to obtain the diffusion coefficient of Li^+ across the printed cathode. Table 3 compares the values of σ_w and D_{Li+} for both the printed electrodes. Despite of a comparable porosity, MC cathode exhibited a diffusion coefficient ($1.85 \times 10^{-13} \text{ cm}^2 \text{s}^{-1}$) about one order of magnitude higher than that of G10 electrode ($1.96 \times 10^{-14} \text{ cm}^2 \text{s}^{-1}$).

Finally, the areal energy and power density were determined for the half-cell assembled with the two 3D-printed cathodes. Indeed, these parameters are affected by the thickness and by the best electron/ion transport of the MC cathode.

In this case, the half-cell provided 32.6 J cm^{-2} energy density with 1 mW cm^{-2} power density, whereas remarkably lower values (6.5 J cm^{-2} and 0.2 mW cm^{-2}) were obtained for the half-cell based on G10. The half-cell assembled with the conventional tape-casted electrode provided even less values (3 J cm^{-2} and 0.1 mW cm^{-2}). The energy and power densities observed for the MC-based half-cell are fully comparable with those obtained for full micro-3D cells,^[23,36] and lower no more than a factor of two if compared to a LMO hybrid 3D-printed electrode with higher thickness ($500 \mu\text{m}$), recently reported in the literature.^[30]

3. Conclusions

For the first time, to our best knowledge, 3D-patterned thick cathodes based on $LiMn_2O_4$ as the active material were produced with an aqueous process by means of robocasting technology. Such a procedure allowed to obtain in very short times (less than 1 minute) cathodes from pastes with high solid loading, and consequently very low solvent amounts, so significantly reducing and simplifying also the drying step and the overall fabrication process.

After a careful screening of green binders and carbon-based additives, two pastes were selected with optimal rheological properties. They enabled to fabricate 3D electrodes with very good printing precision, very good integrity, controlled shape

and geometry. The results indicated that a significant enhancement of the active area of the electrode was achieved with respect of the cathode produced by the conventional tape casting, with remarkable improvement in terms of electrochemical performance.

The presence of carbon black in the additive is mandatory to have good functional properties. The MC printed electrode, in fact, showed superior performance in terms of specific and areal capacity (113 mAhg^{-1} and 2.3 mAhcm^{-2} at 0.1 C) and high areal energy density (32.6 Jcm^{-2}). Compared to the G10 electrode, MC is also more efficient in terms of higher Li ion migration and better electron transport (higher diffusion coefficient, $D_{\text{Li}^+} = 1.85 \times 10^{-13} \text{ cm}^2 \text{s}^{-1}$, and lower charge transfer resistance, $R_{\text{CT}} \approx 94 \Omega \text{cm}^2$).

In summary, the fabrication of 3D-printed electrodes via additive manufacturing is a very promising approach to produce performing electrodes with high loading mass and surface area, which can open the door to develop LIBs with superior areal capacity and energy/power densities. Such a technology also very well fits the use of water as the solvent for paste preparation, making the process safer and more easily scalable at the industrial level.

Acknowledgements

P.M. acknowledges financial support from the Italian Ministry of University and Research (MIUR) through grant "Dipartimenti di Eccellenza – 2017 – Materials for energy".

Conflict of Interest

The authors declare no conflict of interest.

Keywords: lithium-ion batteries • additive manufacturing • robocasting • 3D printing • cathode • LiMn_2O_4

- [1] M. Armand, J.-M. Tarascon, *Nature* **2008**, *451*, 652–657.
- [2] D. Larcher, J.-M. Tarascon, *Nature Chem* **2015**, *7*, 19–29.
- [3] P. K. Nayak, E. M. Erickson, F. Schipper, T. R. Penki, N. Munichandraiah, P. Adelhelm, H. Sclar, F. Amalraj, B. Markovsky, D. Aurbach, *Adv. Energy Mater.* **2018**, *8*, 1702397–1702403.
- [4] L. Wang, B. Chen, J. Ma, G. Cui, L. Chen, *Chem. Soc. Rev.* **2018**, *47*, 6505–6602.
- [5] C. Tealdi, E. Quartarone, P. Mustarelli, in *Rechargeable Batteries: Materials, Technologies and New Trends* (Eds.: Z. Zhang, S. S. Zhang), Springer International Publishing, Cham, 2015, pp. 311–335.
- [6] F. Dou, L. Shi, G. Chen, D. Zhang, *Electrochim. Energ. Rev.* **2019**, *2*, 149–198.

- [7] U.-H. Kim, H.-H. Ryu, J.-H. Kim, R. Mucke, P. Kaghazchi, C. S. Yoon, Y.-K. Sun, *Adv. Energy Mater.* **2019**, *9*, 1803902–1803913.
- [8] H.-M. Cheng, F. Li, *Science* **2017**, *356*, 582–583.
- [9] Y. Kuang, C. Chen, D. Kirsch, L. Hu, *Adv. Energy Mater.* **2019**, *9*, 1901457–1901476.
- [10] M. E. Sotomayor, C. de la Torre-Gamarra, B. Levenfeld, J.-Y. Sanchez, A. Varez, G.-T. Kim, A. Varzi, S. Passerini, *J. Power Sources* **2019**, *437*, 226923–226928.
- [11] L. Hu, F. La Mantia, H. Wu, X. Xie, J. McDonough, M. Pasta, Y. Cui, *Adv. Energy Mater.* **2011**, *1*, 1012–1017.
- [12] X. Wang, Y. Fan, R. Agung Susantyoko, Q. Xiao, L. Sun, D. He, Q. Zhang, *Nano Energy* **2014**, *5*, 91–96.
- [13] B. Bhushan, M. Caspers, *Microsyst Technol* **2017**, *23*, 1117–1124.
- [14] Y. Yang, W. Yuan, X. Zhang, Y. Yuan, C. Wang, Y. Ye, Y. Huang, Z. Qiu, Y. Tang, *Appl. Energy* **2020**, *257*, 114002–114026.
- [15] F. Zhang, M. Wei, V. V. Viswanathan, B. Swart, Y. Shao, G. Wu, C. Zhou, *Nano Energy* **2017**, *40*, 418–431.
- [16] C. Zhu, T. Liu, F. Qian, W. Chen, S. Chandrasekaran, B. Yao, Y. Song, E. B. Duoss, J. D. Kuntz, C. M. Spadaccini, M. A. Worsley, Y. Li, *Nano Today* **2017**, *15*, 107–120.
- [17] X. Tian, J. Jin, S. Yuan, C. K. Chua, S. B. Tor, K. Zhou, *Adv. Energy Mater.* **2017**, *7*, 1700127–1700144.
- [18] M. Wei, F. Zhang, W. Wang, P. Alexandridis, C. Zhou, G. Wu, *J. Power Sources* **2017**, *354*, 134–147.
- [19] M. P. Down, E. M. Martinez-Perinan, C. W. Foster, E. Lorenzo, G. C. Smith, C. E. Banks, *Adv. Energy Mater.* **2019**, *9*, 1803019–1803026.
- [20] C. Liu, F. Xu, X. Cheng, J. Tong, Y. Liu, Z. Chen, C. Lao, J. Ma, *Ceram. Int.* **2019**, *45*, 14188–14197.
- [21] C. Liu, F. Xu, Y. Liu, J. Ma, P. Liu, D. Wang, C. Lao, Z. Chen, *Electrochim. Acta* **2019**, *314*, 81–88.
- [22] C. Sun, S. Liu, X. Shi, C. Lai, J. Liang, Y. Chen, *Chem. Eng. J.* **2020**, *381*, 122641–122649.
- [23] J. Wang, Q. Sun, X. Gao, C. Wang, W. Li, F. B. Holness, M. Zheng, R. Li, A. D. Price, X. Sun, T.-K. Sham, X. Sun, *ACS Appl. Mater. Interfaces* **2018**, *10*, 39794–39801.
- [24] T.-S. Wei, B. Y. Ahn, J. Grotto, J. A. Lewis, *Adv. Mater.* **2018**, *30*, 1703027–1703034.
- [25] A. Zocca, P. Colombo, C. M. Gomes, J. Günster, *J. Am. Ceram. Soc.* **2015**, *98*, 1983–2001.
- [26] Z. Chen, Z. Li, J. Li, C. Liu, C. Lao, Y. Fu, C. Liu, Y. Li, P. Wang, Y. He, *Eur. Ceram. Soc.* **2019**, *39*, 661–687.
- [27] E. Peng, D. Zhang, J. Ding, *Adv. Mater.* **2018**, *30*, 1802404–1802418.
- [28] J. Cesarano, *MRS Proc.* **1998**, *542*, 133–140.
- [29] J. Li, X. Liang, F. Liou, J. Park, *Sci. Rep.* **2018**, *8*, 1846–1857.
- [30] J. Li, M. C. Leu, R. Panat, J. Park, *Mater. Des.* **2017**, *119*, 417–424.
- [31] B. Barry, *Adv. Pharm. Sci.* **1974**, *4*, 1–72.
- [32] S. Nie, W. L. W. Hsiao, Z. Yang, *Int. J. Nanomed.* **2011**, *6*, 151–166.
- [33] T. Marks, S. Trussler, A. J. Smith, D. Xiong, J. R. Dahn, *J. Electrochem. Soc.* **2011**, *158*, A51.
- [34] M. M. Thackeray, *Prog. Solid State Chem.* **1997**, *25*, 1.
- [35] Allen J. Bard and Larry R. Faulkner, *Electrochem. Methods: Fundamentals and Applications*, New York: Wiley, 2001, 2nd ed.
- [36] H. Mazor, D. Golodnitsky, L. Burstein, A. Gladkikh, E. Peled, *J. Power Sources* **2012**, *198*, 264.

Manuscript received: March 18, 2020

Revised manuscript received: April 1, 2020

Accepted manuscript online: April 15, 2020

Version of record online: May 4, 2020